arXiv:1511.02961v3 [cond-mat.mtrl-sci] 17 Dec 2015

Highly Stretchable MoS_2 Kirigami

Paul Z. Hanakata* and David K. Campbell
Department of Physics, Boston University, Boston, MA 02215, USA

Zenan Qi and Harold S. Park
Department of Mechanical Engineering, Boston University, Boston, MA 02215, USA

(Dated: December 18, 2015)

We report the results of classical molecular dynamics simulations focused on studying the mechanical properties of MoS_2 kirigami. Several different kirigami structures were studied based upon two simple non-dimensional parameters, which are related to the density of cuts, as well as the ratio of the overlapping cut length to the nanoribbon length. Our key finding is significant enhancements in tensile yield (by a factor of four) and fracture strains (by a factor of six) as compared to pristine MoS_2 nanoribbons. These results in conjunction with recent results on graphene suggest that the kirigami approach may be a generally useful one for enhancing the ductility of two-dimensional nanomaterials.

Molybdenum disulfide (MoS_2) has been intensely studied in recent years as an alternative two-dimensional (2D) material to graphene. This interest has arisen in large part because (i) MoS_2 exhibits a direct band gap of nearly 2 eV in monolayer form which is suitable for photovoltaics [1]; and (ii) it has recently been explored for many potential applications, ranging from energy storage to valleytonics [2–5].

The mechanical properties of MoS_2 have also been explored recently, through both experimental [6–8] and theoretical methods [9–12]. That MoS_2 has been reported experimentally to be more ductile than graphene [8] naturally raises the critical issue of developing new approaches to enhancing the ductility of 2D materials.

One approach that has recently been proposed towards this end is in utilizing concepts of kirigami, the Japanese technique of paper cutting, in which cutting is used to change the morphology of a structure. This approach has traditionally been applied to bulk materials and recently to micro-scale materials [13–15], though recent experimental [16] and theoretical [17] works have shown the benefits of kirigami for the stretchability of graphene.

Our objective in the present work is to build upon previous successes in applying kirigami concepts to graphene [17] to investigate their effectiveness in enhancing the ductility of a different 2D material, MoS_2, which is structurally more complex than monolayer graphene due to its three-layer structure involving multiple atom types. We accomplish this using classical molecular dynamics (MD) with a recently developed Stillinger-Weber potential [18]. We find that kirigami can substantially enhance the yield and fracture strains of monolayer MoS_2, with increases that exceed those previously seen in monolayer graphene [17].

We performed MD simulations using the Sandia-developed open source code LAMMPS [19, 20] using the Stillinger-Weber potential for MoS_2 of Jiang [18]. All simulations were performed on single-layer MoS_2 sheets. Of relevance to the results in this work, we note that

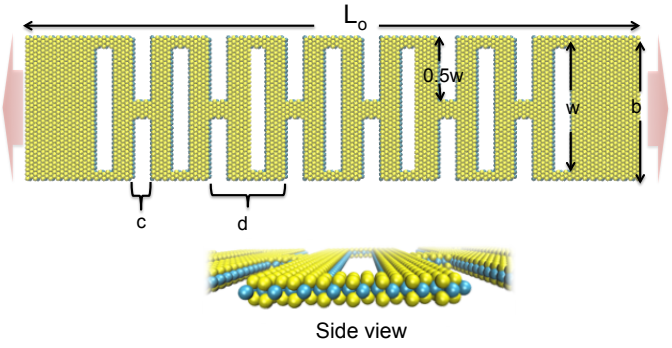

FIG. 1. (Color online) Schematic of the MoS_2 kirigami, with key geometric parameters labeled. The kirigami is deformed via tensile displacement loading that is applied at the two ends in the direction indicated by the arrows. Top image represents a top view of the kirigami.

while the Stillinger-Weber potential does not have a term explicitly devoted to rotations, it does contain two and three-body terms including angular dependencies, which is important for out-of-plane deformations. Furthermore, the Stillinger-Weber potential of Jiang [18] was fit to the phonon spectrum of single-layer MoS_2, which includes both in and out-of-plane vibrational motions. As a result, the Stillinger-Weber potential should do a reasonable job of capturing out-of-plane deformations that involve angle changes, such as rotations.

The MoS_2 kirigami was made by cutting an MoS_2 nanoribbon, which had free edges without additional surface treatment or termination. A schematic view of the kirigami structure and the relevant geometric parameters is shown in Fig. 1. The key geometric parameters are the nanoribbon length L_0, the width b, the height of each interior cut w, the width of each interior cut c, and the distance between successive cuts d. We considered kirigami for both zig-zag (ZZ) and armchair (AC) edges. A representative AC MoS_2 kirigami consisting a number of $N \sim 12,000$ atoms with a nanoribbon length

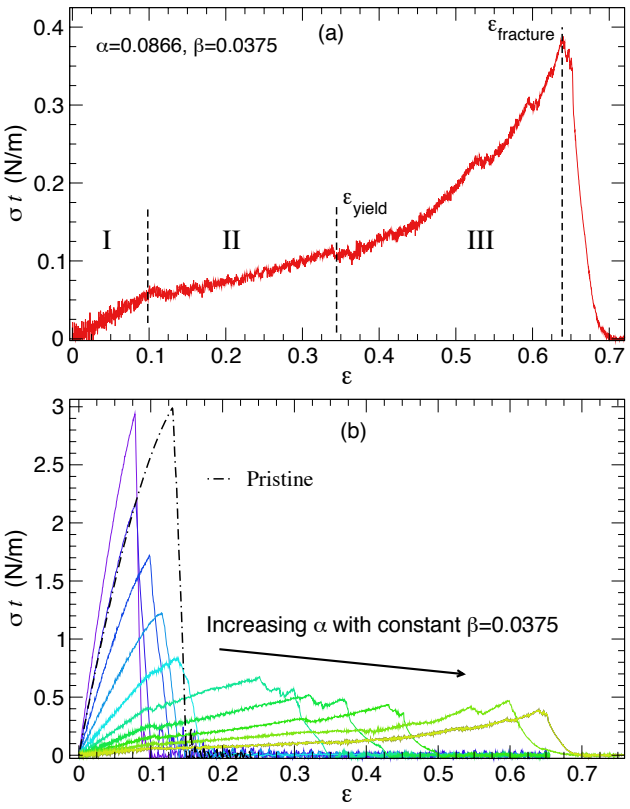

FIG. 2. (Color online) Stress-strain curves of AC MoS_2 kirigami, where the 2D stress was calculated as the stress σ times simulation box t. (a) Stress-strain curve for constant $\alpha = 0.0866$, $\beta = 0.0375$. (b) Stress-strain curve for AC kirigami keeping $\beta = 0.0375$ constant and varying α. Note the brittle fracture of the pristine MoS_2 nanoribbon. In general, the strain in region III increases substantially for $\alpha > 0$.

$L_0 \sim 450$ Å, width $b \sim 100$ Å, height of each interior cut $w \sim 70$ Å, width of each interior cut $c \sim 11$ Å, and distance between successive cuts $d \sim 55$ Å is shown in Fig. 1.

The MD simulations were performed as follows. The kirigami was first relaxed for 200 ps within the NVT (constant number of atoms N, volume V and temperature T) ensemble at low temperature (4.2 K), while non-periodic boundary conditions were used in all three directions. The kirigami was subsequently deformed in tension by applying uniform displacement loading on both ends, such that the kirigami was pulled apart until fracture occurred. We note that in actual applications, the MoS_2 kirigami will likely lie on a substrate, and thus adhesive interactions with the substrate may impact the deformation characteristics. In the present work, we focus on the intrinsic stretchability of the MoS_2 kirigami while leaving the interactions with a substrate for future work.

In addition, we simulated MoS_2 sheets (defined as monolayer MoS_2 with periodic boundary conditions in the plane) and pristine nanoribbons with no cuts for comparative purposes. The calculated fracture strains ϵ_f, fracture stresses σ_f^{3D}, and Young's modulus Y^{3D} are tabulated in Table I. The results are in reasonably good agreement with the experimental and first-principles studies of MoS_2 monolayer sheets [6, 8].[21]

TABLE I. Comparison of mechanical properties of MoS_2 sheets and pristine nanoribbons in the armchair (AC) and zigzag (ZZ) direction.

System	ϵ_f	σ_f^{3D}(GPa)	Y^{3D}(GPa)
Sheet (AC)	0.178	16.8	154.0
Sheet (ZZ)	0.175	15.6	150.7
NR (AC)	0.130	14.6	145.8
NR (ZZ)	0.129	13.6	130.0

In Figure 2 (a), we plot a representative stress-strain curve of MoS_2 kirigami. For this, and the subsequent discussion, we introduce two non-dimensional geometric parameters $\alpha = (w - 0.5b)/L_0$ and $\beta = (0.5d - c)/L_0$, which were also previously used to describe graphene kirigami [17]. α represents the ratio of the overlapping cut length to the nanoribbon length, while β represents the ratio of overlapping width to the nanoribbon length. Put another way, α describes the geometry orthogonal to the loading direction, while β describes the geometry parallel to the loading direction. Figure 2(a) shows the stress-strain for the specific choices of $\alpha = 0.0866$, and $\beta = 0.0375$, which were obtained by choosing b=101.312 Å, L_0=438.693 Å, w=88.648 Å, c=10.967 Å, and d=54.837 Å. In contrast, Figure 2(b) shows the change in the stress-strain response if $\beta = 0.0375$ is kept constant while α changes. This is achieved by changing w while keeping other geometric parameters constant. We also note that the 2D stress was calculated as stress times simulation box size perpendicular to the plane $\sigma \times t$ to remove any issues in calculating the thickness [10], where the stress was obtained using the virial theorem, as is done in LAMMPS.

It can be seen that there are generally three major stages of deformation for the kirigami, as separated by the dashed lines in Fig. 2(a). In the first stage (region I), the deformation occurs via elastic bond stretching, and neither flipping nor rotation of the monolayer MoS_2 sheet is observed as shown in Fig. 3. In previous work, it was found that graphene kirigami rotates and flips in the first stage instead of bond stretching [17]. This does not occur for kirigami in MoS_2 in this first stage because the bending modulus of MoS_2 is nearly seven times higher than that of graphene [10].

In the second stage (region II), for tensile strains (ϵ) exceeding about 10%, further strain hardening occurs. Kirigami patterning allows the MoS_2 monolayer to exhibit out-of-plane deflections, as shown in Fig. 3, which allows the MoS_2 monolayer to undergo additional tensile deformation, which is in contrast to the brittle fracture

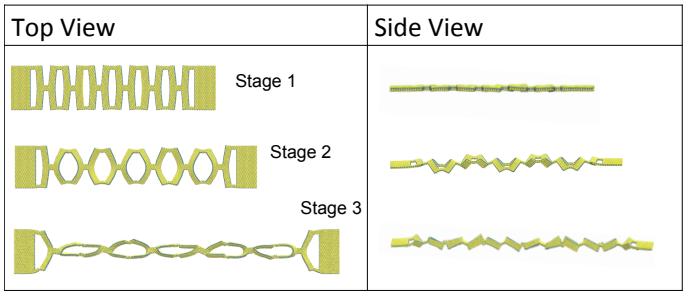

FIG. 3. Side and top views of kirigami during deformation.

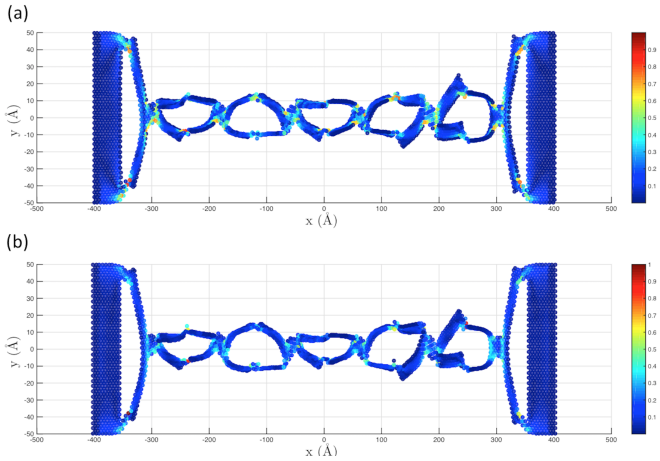

FIG. 4. Von Mises stress prior to the fracture at a tensile strain of 62% in (a) Mo layer and (b) top S layer of kirigami in Fig. 3. We plot the stress distribution layer by layer to give a clear picture of the stress distribution. The von Mises stress were scaled between 0 and 1.

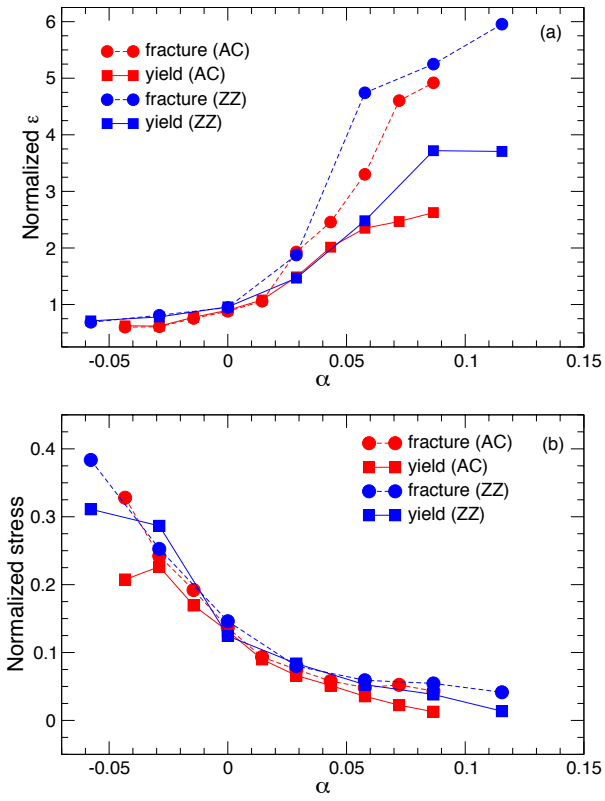

FIG. 5. (Color online) (a) Influence of α on yield and fracture strain for zigzag (ZZ) and armchair (AC) MoS_2 kirigami, with constant $\beta = 0.0375$ for AC and constant $\beta = 0.0417$ for ZZ. (b) Influence of α on yield and fracture stress for zigzag (ZZ) and armchair (AC) MoS_2 kirigami. Data are normalized by MoS_2 nanoribbon results with the same width.

observed for the pristine nanoribbon immediately following the initial yielding event as shown in Fig. 2(b). Furthermore, the out-of-plane deflections cause the slope of the stress-strain curve in region II to be smaller than that in region I. This is because of the change in deformation mechanism from purely elastic stretching of bonds in region I, to a combination of stretching and out of plane buckling in region II.

Local bond breaking near the edges starts to occur at the tensile strain of $\epsilon = 35\%$. The occurrence of bond breaking is usually defined as the yield point, and signifies the demarkation between regions II and III. This local bond breaking occurs due to the concentrated stress at the edges connecting each slab, as previously observed in graphene kirigami [17]. At this stage, each kirigami unit is held by a small connecting ribbon which allows the monolayer to be almost foldable. Fig. 3 (stages 1 to 3) shows how the inner cut surface area having initial area $w \times c$ and the height of the monolayer (largest out-of-plane distance between S atoms) can change significantly during the tensile elongation.

In the final stage, after more than 62.5% tensile strain, fracture and thus failure of the kirigami nanoribbon is observed. Unlike the pristine nanoribbon, the yield point can differ substantially from the fracture strain and the difference increases with increasing cut-overlap, which was described previously as shown in Fig. 2(b). Thus, it is important to quantify the yield point of the kirigami as it defines the beginning of the irreversible deformation regime. Note that these regions vary depending on the kirigami structure as shown in Fig. 2(b).

We also show, in Fig. 4, the von Mises stress distribution prior to fracture at a tensile strain of 62%. In Fig. 4, the stress values were scaled between 0 and 1, and the stress distributions in the top S layer and single Mo layer were plotted separately for ease of viewing as MoS_2 has a tri-layer structure. We found that the largest stresses are concentrated near the edges of the each kirigami unit cell similar to that previously observed in graphene kirigami [17].

Having established the general deformation characteristics for MoS_2 kirigami, we now discuss how the yield and failure characteristics are dependent on the specific

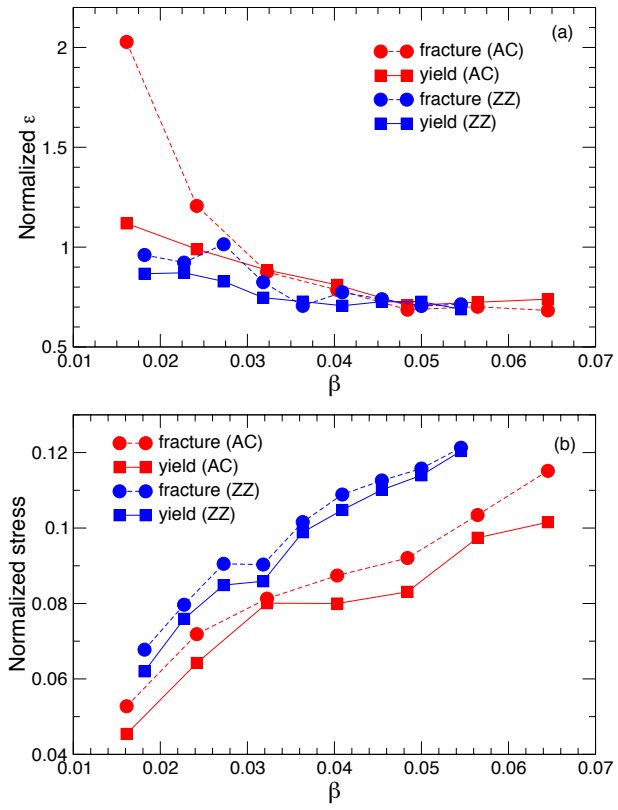

FIG. 6. (Color online) Influence of β on the kirigami yield and fracture strain (a) and stress (b), with constant $\alpha = 0.0186$ for AC and constant $\alpha = 0.0157$ for ZZ. Data are normalized by MoS_2 nanoribbon results with the same width.

kirigami geometry. We discuss the yield and fracture stresses and strains in terms of the two geometric parameters α and β that were previously defined.

The yield strain as a function of α is shown in Fig. 5(a), while the yield stress as a function of α is shown in Fig. 5(b). In these, and all subsequent figures, the stresses and strains are normalized by those for pristine MoS_2 nanoribbons of the same width such that the effect of the kirigami parameters can be directly quantified. As shown in Fig. 5, the MoS_2 kirigami becomes significantly more ductile for $\alpha > 0$, where the zigzag chirality reaches a yield strain that is about a factor of 6 larger than the pristine nanoribbon. In contrast, Fig. 5 (b) shows that the yield stress for kirigami correspondingly decreases dramatically for increasing α. We also note that the kirigami patterning appears to have a similar effect on the ductility of zigzag and armchair MoS_2 kirigami (shown in Fig. 5(a)) as the fracture strain and bending modulus of MoS_2 monolayer sheet in zigzag and armchair direction are similar [10, 18].

The increased ductility occurs because $\alpha = 0$ corresponds to the case when the edge and interior cuts begin to overlap. Increasing α above zero corresponds to when the edge and interior cuts do overlap, and thus it is clear that increasing the overlap increases the ductility of the MoS_2 kirigami. In contrast, the yield stress is higher for smaller α because for negative α, the edge and interior cuts do not overlap, and thus the deformation of the kirigami more closely resembles that of the cut-free nanoribbon.

In addition to the results of α, the effect of β on the kirigami ductility is shown in Figs. 6(a) and 6(b). Specifically, β is varied by changing d while keeping other geometric parameters constant. For both the yield stress and strain, β does impact the yield stress and strain. Increasing β corresponds to an increase in the overlapping region width, which thus results in a smaller yield strain, and increased yield stress as compared to a pristine nanoribbon. For $\beta \geq 0.03$, we do not observe large differences between the AC and ZZ behavior in the case of varying β because increasing β (or decreasing the cut density) makes the kirigami more pristine, leading to similar values of fracture stress and strain in the AC or ZZ direction (see Table I). Our results suggest that the failure strain can be maximized by increasing the overlapping cut (increasing α) and increasing density of the cuts (decreasing β).

Recently, Guo et al. showed stretchability of metal electrodes can be enhanced by creating geometries similar to the ones illustrated in Fig. 1 [15]. Adopting the geometric ratios determining fracture strain described in Ref. [15], we found similar trends: the fracture strain increases with decreasing $\frac{(b-w)}{c}$ and increases with increasing $\frac{b}{d}$. It is interesting to see that a similar trend is operant at a different length scale (an atomically-thin monolayer in this work as compared to a ≈40 nm thin film in the work of Guo et al.), and for a different material system (MoS_2 in this work, nanocrystalline gold in the work of Guo et al.), which suggests that the fracture strain in patterned membranes can be described entirely by geometric parameters.

It is also interesting to note that the yield and fracture strain enhancements shown in Fig. 5(a) exceed those previously reported for monolayer graphene kirigami [17]. The main reason for this is that the failure strain for the normalizing constant, that of a pristine nanoribbon of the same width, is smaller for MoS_2. As shown in Table I, this value is about 13%, whereas the value for a pristine graphene nanoribbon was found to be closer to 30% [17]. However, the largest failure strain for the MoS_2 and graphene kirigami were found to be around 65%, so the overall failure strains for graphene and MoS_2 kirigami appear to reach similar values.

In addition to the yield and fracture behavior, we also discuss the elastic properties, or Young's modulus. For the kirigami system, we expect the Young's modulus to decrease with increasing width of the cut w due to edge effects [9]. Fig. 7 shows the dependence

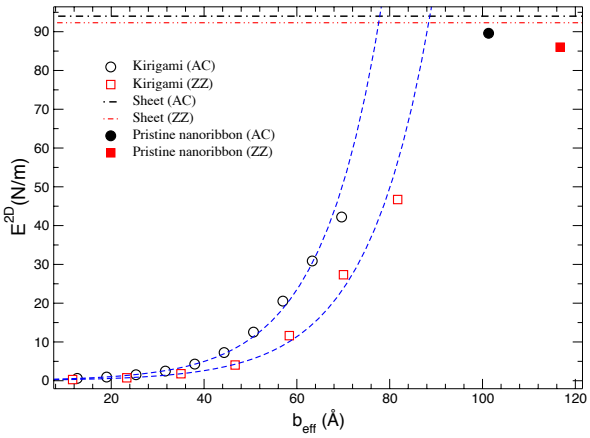

FIG. 7. 2D Young's modulus E^{2D} of armchair (AC) and zigzag (ZZ) kirigami, pristine nanoribbons (PNR), and sheets. Inset shows E^{2D} of kirigami normalized by PNRs. The fitting dashed line (colored blue) is given as a guide to the eye.

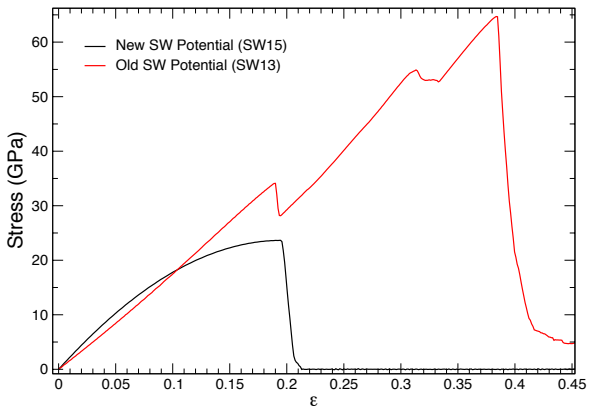

FIG. 8. (Color online) Stress-strain curve of a monolayer MoS_2 sheet under tensile loading along the armchair direction using two different SW potentials. The newer SW potential [18] matches better with the trends observed in DFT calculations [8] than the first SW potential of Jiang et al. [9]. No phase transition is observed with the more recent SW potential of Jiang [18]. For SW13, breaking of bonds between the Mo and S layers occur at $\epsilon \sim 0.2$ and $\epsilon \sim 0.3$ as observed in Ref. [12]

of Young's modulus with effective width $b_{\text{eff}} = b - w$. As can be seen for both armchair and zigzag orientations, the modulus decreases nonlinearly with decreasing effective width, reaching a value that is nearly 200 times smaller than the corresponding bulk value for the smallest effective width value we examined. Furthermore, the trend of the decrease differs from that previously seen in graphene nanoribbons based on first principles calculations [22] and MoS_2 nanoribbons based on atomistic simulations [9], where a significantly more gradual decrease in stiffness was observed. This is due to the fact that for a given nanoribbon width b, the kirigami has significantly more edge area than a nanoribbon, leading to significant decreases in elastic stiffness even for effective widths b_{eff} that are close to the corresponding nanoribbon width.

Before concluding, we note that we have used the more recent Stillinger-Weber (SW15) potential of Jiang [18] rather than the earlier SW potential also developed by Jiang and co-workers [9] (SW13). This is because in comparing the tensile stress-strain curves, the SW15 potential more closely captured the trends observed in DFT calculations [8]. We have also performed simulations of many kirigamis, nanoribbons, and monolayer sheets using the old SW potential. We have found qualitatively similar results *with the very important difference* that the SW13 potential predicts a tensile phase transition in pristine nanoribbon and monolayer sheet [12] that is not observed in the SW15 potential [18]. A comparison of the tensile stress-strain curve for monolayer MoS_2 is shown in Fig. 8 for the potentials of Jiang (SW15) [18], and Jiang et al. (SW13) [9].

In summary, we have applied classical molecular dynamics simulations to demonstrate that the kirigami patterning approach can be used to significantly enhance the tensile ductility of monolayer MoS_2, despite the much higher bending modulus and rather more complex trilayer structure of MoS_2 compared to graphene. The resulting enhancements in tensile ductility are found to exceed those previously reported for graphene [17]. These results suggest that kirigami may be a broadly applicable technique for increasing the tensile ductility of two-dimensional materials generally, and for opening up the possibility of stretchable electronics and photovoltaics using monolayer MoS_2.

P.Z.H. and Z.Q. acknowledge the support of the Physics and Mechanical Engineering Departments at Boston University. D.K.C. is grateful for the hospitality of the Aspen Center for Physics which is supported by NSF Grant #PHY-1066293, and of the International Institute for Physics of the Federal University of Rio Grande do Norte, in Natal, Brazil, where some of this work was completed.

* hanakata@bu.edu

[1] K. F. Mak, C. Lee, J. Hone, J. Shan, and T. F. Heinz, Physical Review Letters **105**, 136805 (2010).
[2] M. Chhowalla, H. S. Shin, G. Eda, L.-J. Li, K. P. Loh, and H. Zhang, Nature Chemistry **5**, 263 (2013).
[3] Q. H. Wang, K. Kalantar-Zadeh, A. Kis, J. N. Coleman, and M. S. Strano, Nature Nanotechnology **7**, 699 (2012).

[4] P. Johari and V. B. Shenoy, ACS Nano **6**, 5449 (2012).
[5] H. Zeng, J. Dai, W. Yao, D. Xiao, and X. Cui, Nature nanotechnology **7**, 490 (2012).
[6] S. Bertolazzi, J. Brivio, and A. Kis, ACS Nano **5**, 9703 (2011).
[7] A. Castellanos-Gomez, M. Poot, G. A. Steele, H. S. J. van der Zant, N. Agrait, and G. Rubio-Bollinger, Advanced Materials **24**, 772 (2012).
[8] R. C. Cooper, C. Lee, C. A. Marianetti, X. Wei, J. Hone, and J. W. Kysar, Physical Review B **87**, 035423 (2013).
[9] J.-W. Jiang, H. S. Park, and T. Rabczuk, Journal of Applied Physics **114**, 064307 (2013).
[10] J.-W. Jiang, Z. Qi, H. S. Park, and T. Rabczuk, Nanotechnology **24**, 435705 (2013).
[11] K. Q. Dang, J. P. Simpson, and D. E. Spearot, Scripta Materialia **76**, 41 (2014).
[12] J. Zhao, L. Kou, J.-W. Jiang, and T. Rabczuk, Nanotechnology **25**, 295701 (2014).
[13] C. F. Guo, T. Sun, Q. Liu, Z. Suo, and Z. Ren, Nature Communications **5**, 3121 (2014).
[14] T. C. Shyu, P. F. Damasceno, P. M. Dodd, A. Lamoureux, L. Xu, M. Shlian, M. Shtein, S. C. Glotzer, and N. A. Kotov, Nature Materials **14**, 785 (2015).
[15] C. F. Guo, Q. Liu, G. Wang, Y. Wang, Z. Shi, Z. Suo, C.-W. Chu, and Z. Ren, Proceedings of the National Academy of Sciences **112**, 12332 (2015).
[16] M. K. Blees, A. W. Barnard, P. A. Rose, S. P. Roberts, K. L. McGill, P. Y. Huang, A. R. Ruyack, J. W. Kevek, B. Kobrin, D. A. Muller, *et al.*, Nature **524**, 204 (2015).
[17] Z. Qi, D. K. Campbell, and H. S. Park, Physical Review B **90**, 245437 (2014).
[18] J.-W. Jiang, Nanotechnology **26**, 315706 (2015).
[19] Lammps, http://lammps.sandia.gov (2012).
[20] S. Plimpton, Journal of Computational Physics **117**, 1 (1995).
[21] In the previous table, 3D stresses $\sigma_{\mathrm{f}}^{\mathrm{3D}}$ are calculated as $\sigma_{\mathrm{f}}^{\mathrm{2D}}/t_{\mathrm{h}}$, where t_{h} is the effective thickness with a value of ~ 6 Å.
[22] P. Wagner, C. P. Ewels, V. V. Ivanovskaya, P. R. Briddon, A. Pateau, and B. Humbert, Physics Review B **84**, 134110 (2011).